

Article

Assessing the Electrochemical Performance of Different Nanostructured CeO₂ Samples as Anodes for Lithium-Ion Batteries

Farah Lamara ¹, Nedjemedine Bounar ¹, Benjamín Solsona ² , Francisco J. Llopis ², María Pilar Pico ³, Daniel Alonso-Domínguez ³, María Luisa López ⁴ and Inmaculada Álvarez-Serrano ^{4,*} 

¹ LIME Laboratory, University M.S.B.Y of Jijel, B.P. 98, Ouled Aissa, Jijel 18000, Algeria; f.lamara@univ-jijel.dz (F.L.); nedjmbounar@yahoo.fr (N.B.)

² Departament d'Enginyeria Química, ETSE, Universitat de València, Av. Universitat s/n, Burjassot, 46100 Valencia, Spain; Benjamin.Solsona@uv.es (B.S.); francisco.llopis@uv.es (F.J.L.)

³ SEPIOL, SA, Polígono Miralcampo, Crta, Nacional II Madrid-Barcelona, Km38.6, Azuqueca de Henares, 19200 Guadalajara, Spain; maria.pico@sepiolsa.com (M.P.P.); Daniel.Alonso@sepiolsa.com (D.A.-D.)

⁴ Departamento Química Inorgánica I, Facultad de Ciencias Químicas, Universidad Complutense de Madrid, Avda, Complutense s/n, 28040 Madrid, Spain; marisal@ucm.es

* Correspondence: ias@ucm.es

Abstract: In this work, six samples of CeO₂ are successfully prepared by diverse synthesis routes leading to different microstructures regarding both morphology and particle size. The structural and microstructural characteristics presented by the samples and their influence on the electrochemical response of the prepared anodes are analyzed. In particular, the Ce-CMK3 sample, synthesized from a mesoporous carbon obtained through a CMK3 silica template, displays an enhanced electrochemical response. Thus, capacity values of ~220 mA h g⁻¹ are obtained at a current rate of 0.155 A g⁻¹ after 50 cycles and an excellent cyclability at intermediate current densities. On the other hand, it is observed that the capacity values are satisfactorily recovered at 0.31 A g⁻¹, displaying ~100 mA h g⁻¹ after 550 cycles and efficiencies close to 100%. The electrochemical performance is interpreted considering the microstructural peculiarities of this anode, which are deeply analyzed.

Keywords: anode materials; cerium oxide; lithium-ion batteries; nanostructured ceria



Citation: Lamara, F.; Bounar, N.; Solsona, B.; Llopis, F.J.; Pico, M.P.; Alonso-Domínguez, D.; López, M.L.; Álvarez-Serrano, I. Assessing the Electrochemical Performance of Different Nanostructured CeO₂ Samples as Anodes for Lithium-Ion Batteries. *Appl. Sci.* **2022**, *12*, 22. <https://doi.org/10.3390/app12010022>

Academic Editor: Gaijin P. Pandey

Received: 25 November 2021

Accepted: 17 December 2021

Published: 21 December 2021

Publisher's Note: MDPI stays neutral with regard to jurisdictional claims in published maps and institutional affiliations.



Copyright: © 2021 by the authors. Licensee MDPI, Basel, Switzerland. This article is an open access article distributed under the terms and conditions of the Creative Commons Attribution (CC BY) license (<https://creativecommons.org/licenses/by/4.0/>).

1. Introduction

At the current moment, both energy storage and transport remain hot topics in the materials research field. Social demand and environmental commitments focus the priorities on the development of future devices. Among other systems, lithium-ion batteries (LIBs) are still nowadays widely employed. Indeed, they have revolutionized human daily life concerning communications, technology, and entertainment [1]. Despite several safety concerns, the rapid technological development of wireless devices and hybrid vehicles in recent years has led to an increased demand for LIBs due to their high power and high energy density [2–5]. Therefore, anode materials have had a growing body of research in the last few years, trying to replace the graphite anode with a new active material that offers higher cycling performance and good capacity retention [6]. The lithiation/de-lithiation process is pivotal for the research of new anode materials with regard to the charging rapidity [7]. The morphology of the nano-sized crystallites of different metal oxides offers new opportunities in materials engineering, due to their improved intrinsic properties. Thus, the reduction in particle size allows engineering the interfacial properties, which directly affect their application domain [8].

Ceria (CeO₂) is an inexpensive and abundant material which has attracted much attention in recent years, as it presents excellent chemical and physical properties. Certainly, it is widely employed in numerous applied fields, such as, among others, catalysts [9–11], oxygen sensors [12,13], fuel cells [14], biotechnology [15], and environmental chemistry [16].

These vast possible applications are due to the outstanding electronic properties of the fluorite-type CeO₂ material. Thus, the Ce oxidation state can change quickly between Ce³⁺ and Ce⁴⁺, which permits to stabilize oxygen vacancies without destructing the structure or modifying it through reversible processes. In addition, ceria can be prepared in numerous microstructured and nanostructured forms, leading to an enhancement of particular applications [17]. Indeed, ceria are used as a dopant to minimize the increase in the internal impedance of different metal-ion batteries, which occurs during discharge [18,19], and it is also extensively studied as a component of the anodes in LIBs. Thus, hollow nanospheres of the CeO₂ material were prepared using anionic micelles [20] and led to good stability and capacity values of about 300 mA h g⁻¹ after 100 cycles at 0.2 A g⁻¹ current rate. The improved performance compared to dense ceria particles was interpreted considering that the hollow morphology favored the lithium insertion–deinsertion processes. Additionally, CeO₂ rhombus and shuttle-shaped microcrystals, obtained by a chemical precipitation method [21], displayed 315 mA h g⁻¹ after 50 cycles at 0.2 mA cm⁻² rate, although for further cycling, the capacity started to fade. Here also the improved response was attributed to small particle size and high concentration of oxygen vacancies. Additionally, other strategies searching the modification of the microstructure were approached. Thus, several doped ceria materials were prepared, e.g., FeO/Mn-rGO [22], displaying an average reversible capacity of over 420 mA h g⁻¹ after 50 cycles at a current of 0.1 C. Moreover, inorganic–organic hybrid composites with ceria nanoparticles on porous carbon were explored as anodes for LIBs, delivering 128 mA h g⁻¹ after 40 cycles at 0.1 A g⁻¹ [23]. The improvement of the electrochemical performance in the prepared anode was attributed to the stabilization of non-aggregated CeO₂ nanoparticles, which favored the electrochemical energy storage by accommodating the volume change of the anode during charge–discharge processes.

On the other hand, the use of a 2D or 3D porous network can lead to significant enhancement in terms of electrochemical properties. Indeed, as they consist of interlinked structures, they favor Li-ions and electron pathways. Thus, the 3D network in a Si@SiOx/C nanoarchitecture (3D-Si@SiOx/C) with nanopores is reported to prevent the volume expansion and to show stable high-temperature cyclability [24]. Redox-active polymer-based materials are shown to be attractive for application in electrochemical devices such as batteries and supercapacitors, with outstanding properties regarding their synthesis, recycling, and excellent processability [25]. In this sense, the use of diverse templates for obtaining mesoporous structures was previously approached [26].

Having in view to obtain an optimized CeO₂ sample for further doping, we are interested in studying in a comparative way the relationship between the electrochemical performance displayed by bare ceria materials and their micro and nanostructure. Our aim is to focus on simple and innocuous synthesis procedures capable to yield ceria samples with different microstructures.

In this paper, we report the characterization of six ceria oxides with different microstructures (labelled as Ce-pH13, Ce-pH7, Ce-ox, Ce-PMMA, Ce-CMK3 and Ce-ref, as explained later) that were prepared by different synthesis routes. Their electrochemical performance as anodes for lithium-ion batteries is assessed and comparatively analyzed.

2. Materials and Methods

2.1. Synthesis Procedures of the Ceria Samples

The CeO₂ samples studied were prepared from cerium nitrate through the following methods.

Ce-pH13 and Ce-pH7 cerium oxides were prepared using a hydrothermal method, using cerium nitrate hexahydrate Ce(NO₃)₃·6H₂O (from MERCK, Madrid, Spain) as a precursor. For Ce-pH13, 30 mmol of Ce(NO₃)₃·6H₂O was added to 0.4 M sodium hydroxide to obtain a solution with pH = 13 stirring vigorously for 30 min. Concerning Ce-pH7 sample, a stoichiometric amount of Ce(NO₃)₃·6H₂O was dissolved in de-ionized water, then ammonia NH₄OH 32% and nitric acid were added until the pH was adjusted to 7, and

the solution was stirred for 1 h. The suspensions were further introduced in autoclaves and heated up to 180 °C for 24 h. Right after, the autoclaves were cooled to room temperature. The mixtures were filtered using a polymeric membrane (polyethersulphone membranes from Sartorius, 200 nm in pore size) and washed several times with de-ionized water and then with alcohol. The filters were dried at 70 °C for 12 h in an oven. These samples were labeled as Ce-pH13 and pH-7, referring to the basic or neutral media employed.

Ce-ox was synthesized by a chemical method using oxalic acid. First, a stirred ethanol solution of cerium nitrate ($\text{Ce}(\text{NO}_3)_3 \cdot 6\text{H}_2\text{O}$ from Sigma Aldrich, Madrid, Spain) was evaporated at 60 °C, and a 1 M solution of oxalic acid was added until precipitation. The solids were dried overnight at 120 °C, and finally calcined in static air for 2 h at 500 °C as previously detailed [11]. This sample was labeled as Ce-ox, underlining the oxalic acid in its synthesis.

Ce-PMMA was synthesized by a physicochemical technique using a polymer soft template. A solution of cerium (III) nitrate was prepared at pH = 4. Then, PMMA was added and stirred to dryness with a further stirring for 1 h and heating at 60 °C. After that, it was calcined at 500 °C for 3 h with a temperature gradient of 0.3 °C/min, as detailed elsewhere [10]. The Ce-PMMA label was chosen, as the poly (methyl methacrylate) polymer was employed in the preparation process.

The Ce-CMK3 material was prepared by infiltration of a cerium nitrate ($\text{Ce}(\text{NO}_3)_3 \cdot 6\text{H}_2\text{O}$ from Sigma Aldrich) solution into a commercial CMK3 carbon, which is a replicate of SBA-15 (from ACS Material, Pasadena, CA, USA). The material was further calcinated in air at 500 °C for total remove of carbon. Given the synthetical origin of the mesoporous carbon employed, this sample was labeled as Ce-CMK3.

The Ce-ref sample was prepared by simple calcination of cerium (III) nitrate (from Sigma Aldrich, Madrid, Spain) in air at 500 °C for 3 h. This sample was taken as a reference, and therefore it was labeled as Ce-ref.

2.2. Characterization Techniques

A PANanalytical X'PERT POWDER diffractometer (Malvern Panalytical Ltd., Malvern, UK) that uses Cu ($K\alpha$) radiation with 1.541874 Å wavelength was used to collect X-ray powder diffraction (XRD) patterns at room temperature.

Nitrogen adsorption measurements were performed on a Micromeritics ASAP 2010 physisorption analyzer at 77 K. Brunauer–Emmett–Teller (BET) and Barret–Joyner–Halenda (BJH) methods were used for the surface area and pore size distribution determination using N_2 adsorption data. Samples were previously outgassed for at least 12 h at 150 °C.

FTIR measurements were carried out in a Two Perkin-Elmer UATR Two spectrophotometer between 400 and 4000 cm^{-1} .

High resolution transmission electron microscopy (HRTEM), images, electron diffraction (ED) patterns and EDX spectra, were acquired in a JEOL 300FEG. The samples were prepared by crushing the powders under n-butanol and dispersing it over copper grids covered with a holey carbon film.

Scanning electron microscope (SEM) images and corresponding EDS spectra were obtained with a JEOL JSM 6335 F microscope. Before SEM examination, the powdered samples were mounted over a carbon film supported onto brass holders and metallized with Au.

For the electrochemical measurements, the anode materials were prepared by mixing 70 wt% of the active material (0.5–3 mg) with 20 wt% of carbon super P (from Imerys Graphite & Carbon, Bironico, Switzerland) and 10 wt% of sodium alginate (from Sigma Aldrich, Madrid, Spain) with a small amount of distilled water and then coated directly on the metal support of a Swagelok cell and dried for a couple of hours. In a dry box filled with argon, all of the Swagelok cell pieces were flocked together starting by the as-prepared coated electrode followed by the fiber sheet from Whatman borosilicate glass (grade GF/D) filled with drops of 1 M LiPF_6 in ethylene carbonate (EC) and dimethyl carbonate (DMC) (1:1 in weight) as the electrolyte, and lithium metal as a counter electrode. Electrochemical

testing was conducted using a Biologic 815 potentiostat. Cyclic voltammetry (CV) and galvanostatic charge and discharge (GCD) tests were conducted in a potential window between 0.01 and 2.5 V. Then, a 0.1 mV/s scan rate was applied for CV testing, and several different currents were used for GCD testing in each case. The applied current densities were normalized to the mass of cerium oxide in the electrode.

3. Results and Discussion

3.1. Structural and Microstructural Characterization

Figure 1 shows the XRD patterns of the prepared ceria oxides in which all the diffraction maxima could be indexed to cubic fluorite-type CeO_2 (PDF 01-078-0694), S.G. $Fm-3m$. Table 1 gathers the cell parameters obtained from Rietveld refinements of these data, by means of the Fullprof program. In the Supplementary Materials file, Figure S1 shows the corresponding fits for representative cases and Table S1 includes the corresponding R-factors. The crystallinity of the samples significantly varies depending on the synthesis route employed. Thus, it is clearly appreciated that the Ce-pH13 and Ce-CMK3 samples present smaller width of the XRD diffraction maxima. The corresponding crystallite sizes in each case as obtained from the Scherrer formula are also included in Table 1.

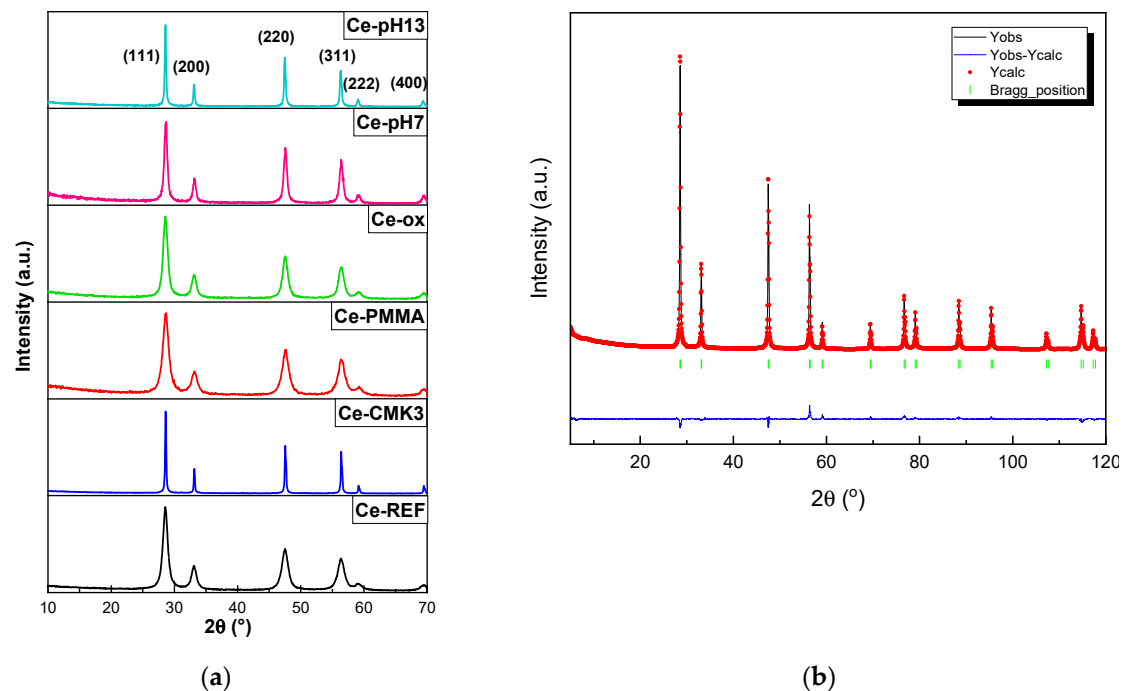


Figure 1. (a) XRD diffraction patterns for prepared the ceria materials. The indexation refers to CeO_2 fluorite-type (PDF 01-078-0694); (b) Rietveld profiles and R-factors for the Ce-CMK3 sample.

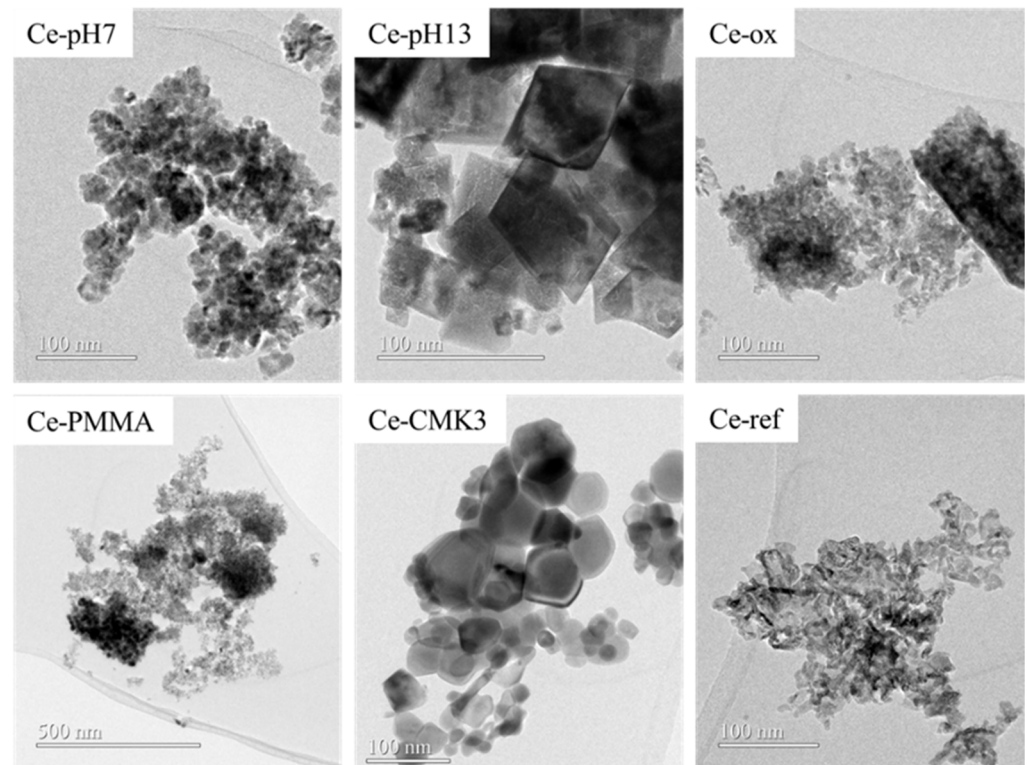
Textural features of the ceria compounds were studied by means of nitrogen adsorption measurements. The corresponding specific surface area (S_{BET}) values are included in Table 1. In alignment with the XRD results, the observed different widening of the diffraction peaks is related to the crystallite sizes. Thus, the smaller crystallite sizes fit with the higher surface areas observed.

The microstructure of the studied ceria compounds was analyzed by HRTEM. Figure 2 shows representative low magnification images. Relevant differences concerning particle morphology and size can be appreciated. Indeed, whereas Ce-pH7, Ce-PMMA, Ce-ox and Ce-ref show very small particles of predominant mean sizes of about 3 nm, which tend to aggregate, in Ce-pH13 and Ce-CMK3 samples most particles are of about 100 nm.

Table 1. Cell parameters, crystallite sizes and S_{BET} values for the ceria samples.

Notation	Synthesis Method	Crystallite Size (nm) ^b	a (Å)	S_{BET} ($\text{m}^2 \text{g}^{-1}$) ^c	Particle Size Range (nm) ^d
Ce-pH13	Hyd ^a , pH = 13	34.3	5.4244 (2)	9	10–100
Ce-pH7	Hyd ^a , pH = 7	15.0	5.4186 (2)	42	3–18
Ce-ox	Oxalate precursor	9.5	5.4144 (7)	14.1	2–15
Ce-PMMA	PMMA template	8.2	5.4159 (9)	120	2–20
Ce-CMK3	CMK3 template	42.8	5.4123 (1)	7	15–130
Ce-Ref	Calcination	9.4	5.4175 (7)	24.1	3–15

^a Refers to hydrothermal. ^b From XRD data. ^c Specific surface area. ^d From HRTEM.

**Figure 2.** Representative low-magnification HRTEM images of the ceria samples.

The particle size ranges of the samples are included in Table 1. It can be appreciated that these values are coherent with those obtained from the Scherrer expression. Rigorously, the Scherrer expression gives the coherent diffraction domain size, rather than crystallite size or particle size. Nevertheless, in absence of relevant strain and disorder effects, the order of magnitude of both should be comparable. In our samples, both effects, if present, should be similar. In Figure 3, representative high magnification images of Ce-pH7, Ce-pH13 and Ce-CMK3 are shown. As can be observed, the ED patterns included are coherent with the particle's sizes in each case.

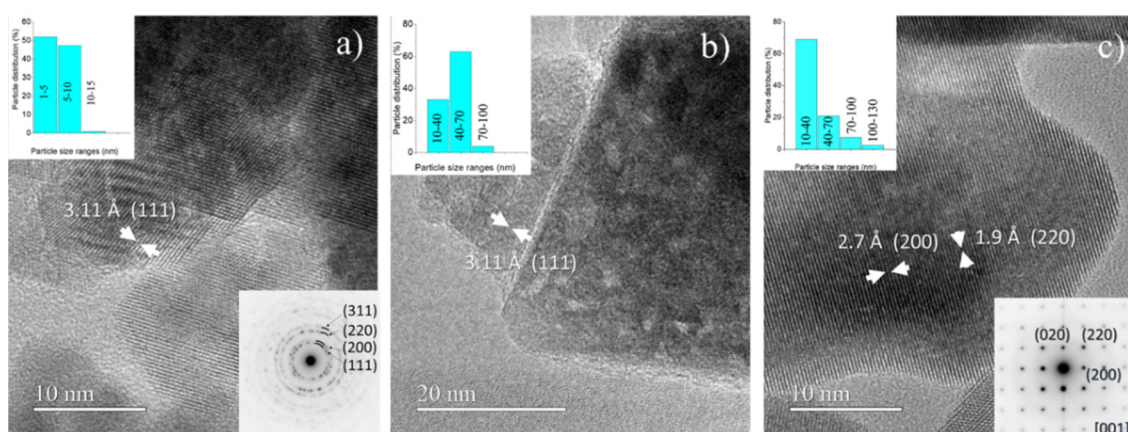


Figure 3. High-magnification images, corresponding ED patterns and particle size distribution for (a) Ce-pH7, (b) Ce-pH13 and (c) Ce-CMK3 samples.

Morphological differences are also evident among the samples. Thus, pseudo-spherical particles are obtained in the Ce-CMK3 sample, whereas polygonal-rhombic particles are present in Ce-pH13. Moreover, nanovesicles typical of samples obtained by hydrothermal methods are also observed in Ce-pH13. The shape of the tiny, aggregated nanoparticles of Ce-pH7, Ce-PMMA and Ce-ox is pseudo-spherical, whereas they present a bar-like morphology in the Ce-ref sample. Therefore, the CeO₂ compound prepared by different synthesis routes clearly shows different microstructures. In the case of Ce-CMK3, the particle size distribution is somewhat more monodisperse, and the aggregation phenomenon is not appreciated. Figure S2 (in the Supplementary Materials file) includes representative EDX spectra for all the samples. In the case of the Ce-CMK3 anode, small amounts of silicon are detected, probably already present in the carbonaceous material employed in its preparation, which was obtained from a treatment over a CMK3 silica template.

FTIR experiments were carried out to analyze the possible different functional groups appearing in the samples because of the different synthesis procedures. Figure S3 of the Supplementary Materials file shows the corresponding spectra between 4000 and 400 cm⁻¹ for the prepared materials. The obtained bands are in good agreement with the literature [20,27]. The strong absorption bands observed between 3000 and 4000 cm⁻¹ correspond to physisorbed water (O–H stretching). The bands appearing between 1400 and 2000 cm⁻¹ may appear from the absorption of atmospheric CO₂ or carbonates at the surface. The absorption bands appearing in all the samples at less than 800 cm⁻¹ are related to the metal–oxygen stretching (Ce–O stretch). In general, the hydrothermally obtained samples are richer in water and in adsorbed carbon dioxide, as expected. A small peak of N–H is observed in the Ce-pH7 sample, in coherence with the synthesis process which includes ammonia. In the Ce-CMK3 sample, the absence of bands corresponding to Si–O confirms that the mesoporous CMK3 silica used in the preparation of the carbon employed in the synthesis procedure of the anode was adequately removed. In this sense, the very low Si content observed by EDX in this sample should not be taken as significant.

3.2. Electrochemical Characterization

Figure 4 shows selected discharge–charge curves at 0.155 A g⁻¹ current rate, for all the ceria anodes studied. Table 2 gathers the corresponding first cycle capacity values and the ranges of capacity values displayed in each case (i.e., minimum and maximum values obtained in the range of cycles explored in each case). Figure S4 (Supplementary Materials file) includes a comparison of discharge and charge capacity values vs. cycle number in the first 50 cycles for all the ceria anodes.

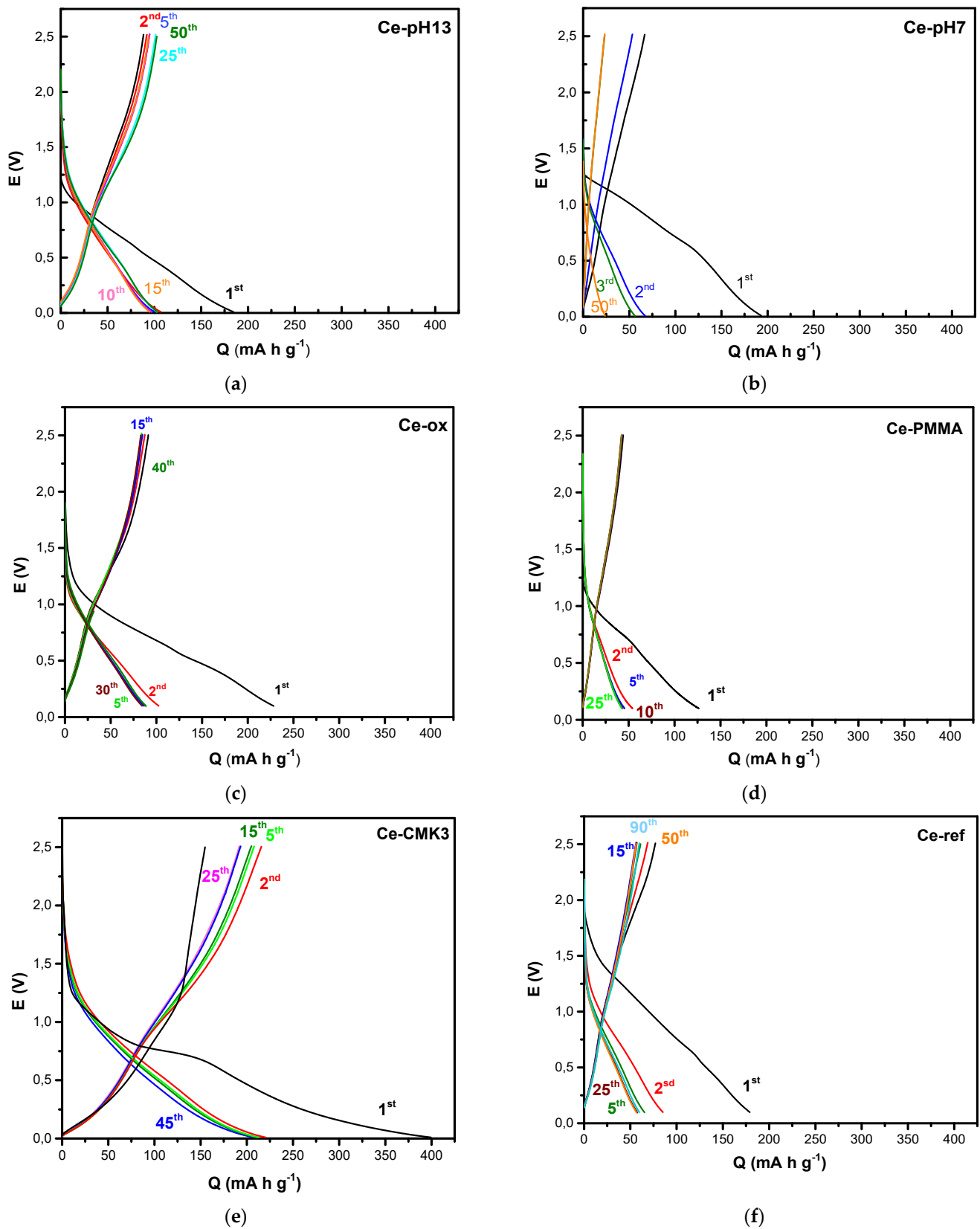


Figure 4. Selected discharge–charge curves at 0.155 A g^{-1} current rate for (a) Ce-pH13, (b) CepH7, (c) Ce-ox, (d) Ce-PMMA, (e) Ce-CMK3 and (f) Ce-ref.

Table 2. First cycle discharge capacity (Q_d) and range of capacity values displayed for the ceria samples.

Sample	Q_d 1st Cycle (mA h g^{-1})	Q_d at 0.155 A g^{-1} (mA h g^{-1}) *
Ce-pH13	184	91 (15)–103 (2)
Ce-pH7	193	24 (50)–67 (2)
Ce-ox	227	85 (30)–102 (2)
Ce-PMMA	108	43 (25)–56 (2)
Ce-CMK3	401	212 (45)–226 (2)
Ce-ref	179	58 (50)–85 (2)

* The numbers in bold and brackets refer to corresponding cycle.

In all the cases, the first discharge cycle displays a much greater capacity values than those obtained in following cycles. This behavior is typically obtained in previously reported cycling curves and can be related to the formation of a solid electrolyte interphase (SEI) film and the insertion of Li^+ into CeO_2 [28]. Indeed, the development of such a film protects the device from further capacity losses in the successive cycles. This phenomenon is characteristic of various electrochemical metal-ion systems, e.g., Li-ion and Na-ion batteries [29]. The Ce-ref, Ce-PMMA and Ce-pH7 anodes display moderate capacity values close to 60 mA h g^{-1} at 0.155 A g^{-1} current density, which is comparable to values previously obtained for dense CeO_2 particles [20]. The Ce-ox and Ce-pH13 anodes present higher capacity values of about 100 mA h g^{-1} at the same intermediate current rate, also in the range of typical values obtained for bare CeO_2 samples [30]. Among the different anodes studied, the highest performance is clearly displayed by the Ce-CMK3 sample, which presents capacity values of about 200 mA h g^{-1} through the first 45 cycles. This response is more performative than that previously reported for bare ceria samples [30] and ceria anodes prepared on porous carbon templates [23]. Nevertheless, if the application in a real device was foreseen, the electrochemical performance of this bare ceria should be enhanced by processing of the anode. Indeed, as indicated above, in the present work, we aimed to comparatively assess the characteristics of different bare ceria materials in order to select the most adequate for further preparation of different composites, mainly with non-toxic and abundant iron and manganese oxides. In this sense, the Ce-CMK3 anode is revealed as the most adequate.

In Figure 5, the cyclic voltammetry (CV) curves (from 1st to 4th cycles) in the voltage region of 0.01–3.0 V vs. Li/Li^+ at a 0.1 mV/s rate for the Ce-CMK3 anode are shown. As can be appreciated, the first cycle is partially irreversible because of side reactions, such as electrolyte decomposition and the formation of the SEI film, as indicated before in previous works [31]. The CV curves quickly become stable, and the discharge–charge curves almost overlap with each other, indicating that the electrochemical reactions are highly reversible for our ceria anode. A strong cathodic peak is observed at the first cycle at $\sim 0.7 \text{ V}$, which could be ascribed to the formation of SEI film and the insertion of Li^+ into CeO_2 , as previously suggested [28]. Thus, in following cycles, it reduces in intensity and shifts toward $\sim 0.5 \text{ V}$. Although the response in the first cycle is somewhat rough, a broad anodic peak at $\sim 1.2 \text{ V}$ could be related to the extraction of Li^+ from the CeO_2 host. This broad signal is sharpened and shifted toward $\sim 1.4 \text{ V}$, indeed corresponding to the delithiation process, in coherence with previous reported data for ceria anodes [22,28].

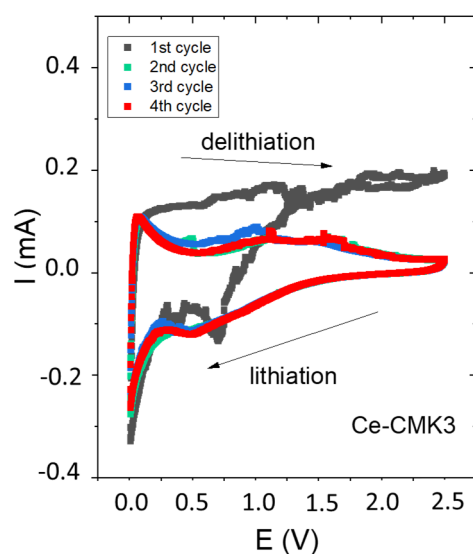
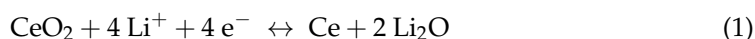
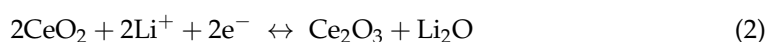


Figure 5. CV curves (from 1st to 4th cycles) for the Ce-CMK3 anode in the voltage range of 0.01–3.0 V vs. Li/Li⁺ at 0.1 mV/s rate.

Several redox processes were reported in the last years to probably operate in the CeO₂–Li system. For example, in the previous work of Su et al. [32], the authors took into account, as examples, the processes operating in CuO and Co₃O₄ anodes in which the oxidation states of the metal cations reduce to zero from the highest value after reaction with Li (i.e., conversion anodes). Thus, admitting that basic electrochemical reaction of ceria in LIBs was still unknown, they started from the initial hypothesis of considering the ceria anode as a conversion anode. The reactions of the reversible lithiation/delithiation process in this case would be



However, from in situ transmission electron microscopy analysis, a reversible phase transformation between fluorite CeO₂ and cubic Ce₂O₃ was eventually concluded:



This conclusion was drawn from experimental data obtained in a nano LIB device constructed by CeO₂/graphene electrode, a layer of Li₂O solid electrolyte, and a bulk Li metal (counter electrode inside the TEM). As similar results of in situ experiments on carbon nanotubes and graphene nanoribbons were obtained, it was concluded that this could be an intrinsic property regarding the interaction between lithium and exposed graphite basal planes.

However, several years later, both Li et al. [33] and Su et al. [28], from SXRD, high resolution XPS and DFT, proved that the lithiated ceria phases, in which the reduction of Ce(IV) to Ce(III) takes place, own the same fluorite structure. In both cases, the anode composites included different carbonaceous additives, such as those employed in our case. The obtained CV profiles were also similar to those we obtained. The corresponding reaction is



We, therefore, assumed this mechanism as operative in our case, although the small amount of active material (0.5–3 mg in conventional Swagelok-type cells) impeded us to unambiguously determine whether the post-cycling structure was maintained or not.

In this process, the fluorite structure of CeO₂ is maintained, whereas a lattice parameter expansion of less than 1.9% takes place for x values of about 0.375. Interestingly, after the

first cycle, the CV curves for the battery with the Ce-CMK3 anode become smooth and coincident, suggesting a charge–discharge process with good reversibility.

Aiming to further analyze the performance of the Ce-CMK3 anode, a long-term cycling experiment was carried out. Figure 6 shows the charge–discharge capacities through cycling up to 550 cycles at different current rates and selected E vs. Q curves. Although the capacity values are achieved at moderate compared to previous reported nanoarchitected ceria anodes [20,22], it must be underlined that the Ce-CMK3 anode displays excellent cyclability particularly at moderate high current densities. Thus, after 400 cycles at different rates, the capacity values are practically recovered when cycling again at 0.31 A g^{-1} up to 500 cycles (Figure 6b), with efficiencies close to 100%. The improved cyclability was previously connected to microstructural aspects. Thus, small particle size or porous nature of the material could increase the electrode–electrolyte surface area and increase the amount of oxygen vacancies, leading to a better electrochemical response [21].

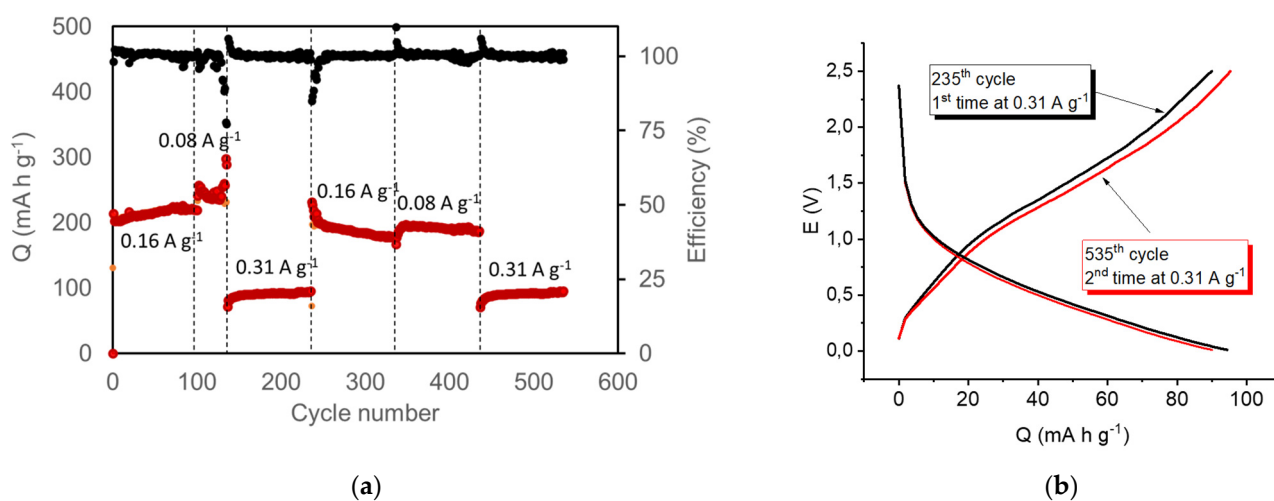


Figure 6. Long-term cycling for Ce-CMK3 anode: (a) Q vs. cycle number at different current rates and (b) selected E vs. Q curves at 0.31 A g^{-1} .

In this sense, the enhanced long-term cyclability of Ce-CMK3 anode could be related to its microstructure features. Although it does not present particularly small particle size when compared to the other prepared anodes, the particles do not aggregate, and probably the Li^+ and e^- pathways are favored. Indeed, a deeper inspection from HRTEM analysis reveals interesting microstructural details of Ce-CMK3 particles, as shown in Figure 7. First, a nanoarchitecture regarding the particles from the surface to the bulk can be appreciated (Figure 7a,b), i.e., an outer part of 3–4 nm is visible. Second, as mentioned above, particles do not aggregate as they do in the other ceria samples. Instead, particles are well interconnected.

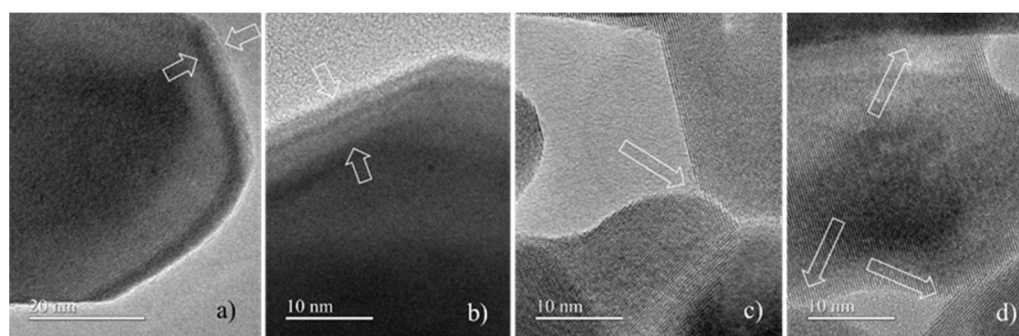


Figure 7. High magnification HRTEM images showing Ce-CMK3 particles in detail: arrows indicate nanoarchitecture regarding surface particle in (a,b); and contact between particles in (c,d).

On the other hand, SEM images also evidence particularities of the Ce-CMK3 anode. Figure 8 shows several micrographs at different magnifications. In them, the existence of great pores of about 200 nm is apparent throughout all the sample. A closer inspection evidences the structure of such cavities (Figure 8c). Thus, the well-connected particles form holes which are separated from each other by about 1 μm . These formations are probably the result of the calcination process applied to the Ce-CMK3 sample for oxidizing the mesoporous carbon employed in the synthesis method. In summary, the Ce-CMK3 anode presents several microstructural peculiarities which could be connected to its enhanced cyclability.

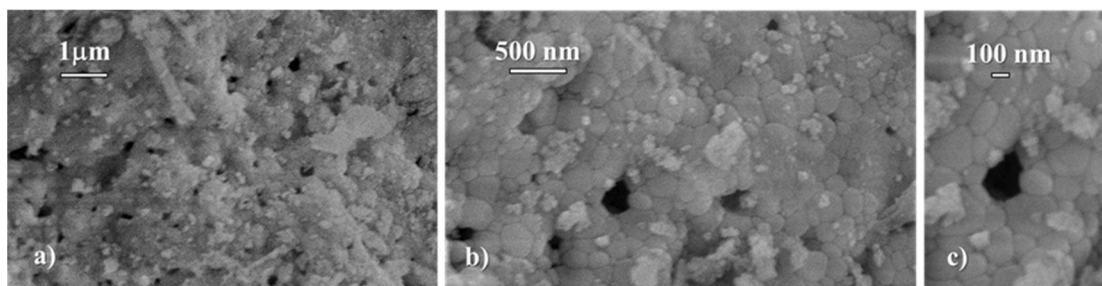


Figure 8. SEM images of Ce-CMK3 sample at different magnifications showing (a) cavities separated from each other by distances of about 1 μm , (b) well-connected particles forming the cavities, (c) a detailed view of a cavity.

In this sense, considering that CeO_2 material is non-toxic, low cost and environmentally friendly, our nanostructured bare CeO_2 anode is a promising candidate to improve the capacity values by doping.

Supplementary Materials: The following are available online at <https://www.mdpi.com/article/10.3390/app12010022/s1>, Figure S1: Rietveld profiles for (a) Ce-pH7 and (b) Ce-pH-13. Red points refer to the experimental data, black lines to the calculated profile, blue line indicate the difference between them and vertical green lines indicate the Bragg reflections, Table S1: Rietveld factors from the refinements for the ceria anodes. Figure S2: Representative EDX spectra for the ceria anodes. Figure S3: Representative FTIR spectra for the ceria anodes. Figure S4: Comparative of charge (pale color) and discharge (intense color) capacity values during the first 50 cycles at 0.155 A g^{-1} current rate for all the ceria anodes.

Author Contributions: Conceptualization, I.Á.-S. and F.L.; methodology, M.L.L. and B.S.; software, N.B. and M.P.P.; validation, F.J.L. and D.A.-D.; investigation, I.Á.-S. and M.L.L. writing—original draft preparation, I.Á.-S. and F.L.; writing—review and editing, M.L.L. and B.S.; visualization, F.L.; supervision, M.L.L.; project administration, M.L.L.; funding acquisition, I.Á.-S. All authors have read and agreed to the published version of the manuscript.

Funding: This work was supported by the Spanish Ministry of Economy and Competitiveness (MINECO) through projects MAT2017-84118-C2-2-R and MAT2017-84118-C2-1-R, which role does not concern any aspect regarding study design, the collection, analysis and interpretation of data, the writing of the report or the decision to submit the article for publication.

Institutional Review Board Statement: Not applicable.

Informed Consent Statement: Not applicable.

Acknowledgments: Authors would like to thank Imerys Graphite & Carbon who kindly provided the carbon black. In addition, authors are grateful to the CAI centers of UCM (XRD and electron microscopy).

Conflicts of Interest: The authors declare no conflict of interest. The funders had no role in the design of the study; in the collection, analyses, or interpretation of data; in the writing of the manuscript, or in the decision to publish the results.

References

1. Weiss, M.; Ruess, R.; Kasnatscheew, J.; Levartovsky, Y.; Levy, N.R.; Minnmann, P.; Stolz, L.; Waldmann, T.; Wohlfahrt-Mehrens, M.; Aurbach, D.; et al. Fast Charging of Lithium-Ion Batteries: A Review of Materials Aspects. *Adv. Energy Mater.* **2021**, *11*, 2101126. [[CrossRef](#)]
2. Poizot, P.; Laruelle, S.; Grugeon, S.; Dupont, L.; Tarascon, J.-M. Nano-sized transition-metal oxides as negative-electrode materials for lithium-ion batteries. *Nature* **2000**, *407*, 496–499. [[CrossRef](#)] [[PubMed](#)]
3. Vetter, J.; Novák, P.; Wagner, M.R.; Veit, C.; Möller, K.-C.; Besenhard, J.O.; Winter, M.; Wohlfahrt-Mehrens, M.; Vogler, C.; Hammouche, A. Ageing mechanisms in lithium-ion batteries. *J. Power Sources* **2005**, *147*, 269–281. [[CrossRef](#)]
4. Huang, Y.-H.; Park, K.-S.; Goodenough, J.B. Improving Lithium Batteries by Tethering Carbon-Coated LiFePO₄ to Polypyrrole. *J. Electrochem. Soc.* **2006**, *153*, A2282. [[CrossRef](#)]
5. Chen, Y.; Kang, Y.; Zhao, Y.; Wang, L.; Liu, J.; Li, Y.; Liang, Z.; He, X.; Li, X.; Tavajohi, N.; et al. A review of lithium-ion battery safety concerns: The issues, strategies, and testing standards. *J. Energy Chem.* **2021**, *59*, 83–99. [[CrossRef](#)]
6. Gong, Q.; Gao, T.; Huang, H.; Wang, R.; Cao, P.; Zhou, G. Double-shelled CeO₂@C hollow nanospheres as enhanced anode materials for lithium-ion batteries. *Inorg. Chem. Front.* **2018**, *5*, 3197–3204. [[CrossRef](#)]
7. Aziam, H.; Tamraoui, Y.; Ma, L.; Amine, R.; Wu, T.; Manoun, B.; Xu, G.L.; Amine, K.; Alami, J.; Saadoune, I. Mechanism of the First Lithiation/Delithiation Process in the Anode Material CoFeOPO₄@C for Li-Ion Batteries. *J. Phys. Chem. C* **2018**, *122*, 7139–7148. [[CrossRef](#)]
8. Chavali, M.S.; Nikolova, M.P. Metal oxide nanoparticles and their applications in nanotechnology. *SN Appl. Sci.* **2019**, *1*, 607. [[CrossRef](#)]
9. Lykaki, M.; Pachatouridou, E.; Iliopoulou, E.; Carabineiro, S.A.C.; Konsolakis, M. Impact of the synthesis parameters on the solid state properties and the CO oxidation performance of ceria nanoparticles. *RSC Adv.* **2017**, *7*, 6160–6169. [[CrossRef](#)]
10. Solsona, B.; Sanchis, R.; Dejoz, A.; Garcia, T.; Rodríguez, L.; Nieto, J.M.; Cecilia, J.A.; Rodríguez-Castellon, E. Total Oxidation of Propane Using CeO₂ and CuO-CeO₂ Catalysts Prepared Using Templates of Different Nature. *Catalysts* **2017**, *7*, 96. [[CrossRef](#)]
11. Solsona, B.; Concepción, P.; Hernández, S.; Demicol, B.; Nieto, J.M.L. Oxidative dehydrogenation of ethane over NiO-CeO₂ mixed oxides catalysts. *Catal. Today* **2012**, *180*, 51–58. [[CrossRef](#)]
12. Jasinski, P.; Suzuki, T.; Anderson, H.U. Nanocrystalline undoped ceria oxygen sensor. *Sens. Actuators B Chem.* **2003**, *95*, 73–77. [[CrossRef](#)]
13. Primo, A.; Marino, T.; Corma, A.; Molinari, R.; García, H. Efficient Visible-Light Photocatalytic Water Splitting by Minute Amounts of Gold Supported on Nanoparticulate CeO₂ Obtained by a Biopolymer Templating Method. *J. Am. Chem. Soc.* **2011**, *133*, 6930–6933. [[CrossRef](#)]
14. Wang, B.; Zhu, B.; Yun, S.; Zhang, W.; Xia, C.; Afzal, M.; Cai, Y.; Liu, Y.; Wang, Y.; Wang, H. Fast Ionic Conduction in Semiconductor CeO_{2-δ} Electrolyte Fuel Cells. *NPG Asia Mater.* **2019**, *11*, 1–12. [[CrossRef](#)]
15. Tarnuzzer, R.W.; Colon, J.; Patil, S.; Seal, S. Vacancy Engineered Ceria Nanostructures for Protection from Radiation-Induced Cellular Damage. *Nano Lett.* **2005**, *5*, 2573–2577. [[CrossRef](#)] [[PubMed](#)]
16. Salaev, M.; Salaeva, A.; Kharlamova, T.; Mamontov, G. Pt-CeO₂-based composites in environmental catalysis: A review. *Appl. Catal. B Environ.* **2021**, *295*, 120286. [[CrossRef](#)]
17. Yang, S.; Gao, L. Controlled Synthesis and Self-Assembly of CeO₂ Nanocubes. *J. Am. Chem. Soc.* **2006**, *128*, 9330–9331. [[CrossRef](#)]
18. Minakshi, M.; Nallathamby, K.; Mitchell, D.R. Electrochemical characterization of an aqueous lithium rechargeable battery: The effect of CeO₂ additions to the MnO₂ cathode. *J. Alloys Compd.* **2009**, *479*, 87–90. [[CrossRef](#)]
19. Minakshi, M.; Mitchell, D.R.G.; Carter, M.L.; Appadoo, D.; Nallathamby, K. Microstructural and Spectroscopic Investigations into the Effect of CeO₂ Additions on the Performance of a MnO₂ Aqueous Rechargeable Battery. *Electrochim. Acta* **2009**, *54*, 3244–3249. [[CrossRef](#)]
20. Sasidharan, M.; Gunawardhana, N.; Yoshio, M.; Nakashima, K. CeO₂ Hollow Nanospheres as Anode Material for Lithium Ion Batteries. *Chem. Lett.* **2012**, *41*, 386–388. [[CrossRef](#)]
21. Liu, H.; Le, Q. Synthesis and performance of cerium oxide as anode materials for lithium ion batteries by a chemical precipitation method. *J. Alloys Compd.* **2016**, *669*, 1–7. [[CrossRef](#)]
22. Ogunniran, K.O.; Murugadoss, G.; Thangamuthu, R.; Nishanthi, S.T. Nanostructured CeO₂/FeO₃/Mn-RGO Composite as Anode Material in Li-Ion Battery. *J. Alloys Compd.* **2019**, *786*, 873–883. [[CrossRef](#)]
23. Kim, H.; Shuvo, M.A.I.; Karim, H.; Noveron, J.C.; Tseng, T.-L.; Lin, Y. Synthesis and characterization of CeO₂ nanoparticles on porous carbon for Li-ion battery. *MRS Adv.* **2017**, *2*, 3299–3307. [[CrossRef](#)]
24. Lee, J.; Moon, J.; Han, S.A.; Kim, J.; Malgras, V.; Heo, Y.-U.; Kim, H.; Lee, S.-M.; Liu, H.K.; Dou, S.X.; et al. Everlasting Living and Breathing Gyroid 3D Network in Si@SiO_x/C Nanoarchitecture for Lithium Ion Battery. *ACS Nano* **2019**, *13*, 9607–9619. [[CrossRef](#)] [[PubMed](#)]
25. Kim, J.; Kim, J.H.; Ariga, K. Redox-Active Polymers for Energy Storage Nanoarchitectonics. *Joule* **2017**, *1*, 739–768. [[CrossRef](#)]
26. Cheng, C.; Chen, F.; Yi, H.; Lai, G. CeO₂ mesoporous microspheres for high performance supercapacitors and lithium-ion batteries. *J. Energy Storage* **2021**, *35*, 102305. [[CrossRef](#)]
27. Jayakumar, G.; Irudayaraj, A.A.; Raj, A.D. Investigation on the synthesis and photocatalytic activity of activated carbon-cerium oxide (AC-CeO₂) nanocomposite. *Appl. Phys. A* **2019**, *125*, 742. [[CrossRef](#)]

28. Sun, J.; Li, B.; Jin, C.; Peng, L.; Dai, D.; Hu, J.; Yang, C.; Lu, C.; Yang, R. Construction of 3D porous CeO₂ ceramic hosts with enhanced lithiophilicity for dendrite-free lithium metal anode. *J. Power Sources* **2021**, *484*, 229253. [[CrossRef](#)]
29. Minakshi, M.; Mitchell, D.R.G.; Munnangi, A.R.; Barlow, A.J.; Fichtner, M. New insights into the electrochemistry of magnesium molybdate hierarchical architectures for high performance sodium devices. *Nanoscale* **2018**, *10*, 13277–13288. [[CrossRef](#)]
30. Ma, Y.; Ma, Y.; Giuli, G.; Euchner, H.; Groß, A.; Lepore, G.O.; d’Acapito, F.; Geiger, D.; Biskupek, J.; Kaiser, U.; et al. Introducing Highly Redox-Active Atomic Centers into Insertion-Type Electrodes for Lithium-Ion Batteries. *Adv. Energy Mater.* **2020**, *10*, 2000783. [[CrossRef](#)]
31. Shi, Y.; Fu, J.; Hui, K.; Liu, J.; Gao, C.; Chang, S.; Chen, Y.; Gao, X.; Gao, T.; Xu, L.; et al. Promoting the Electro-chemical Properties of Yolk-Shell-Structured CeO₂ Composites for Lithium-Ion Batteries. *Microstructures* **2021**, *1*, 2021005.
32. Su, Q.; Chang, L.; Zhang, J.; Du, G.; Xu, B. In Situ TEM Observation of the Electrochemical Process of Individual CeO₂/Graphene Anode for Lithium Ion Battery. *J. Phys. Chem. C* **2013**, *117*, 4292–4298. [[CrossRef](#)]
33. Li, K.; Zhou, X.; Nie, A.; Sun, S.; He, Y.-B.; Ren, W.; Li, B.; Kang, F.; Kim, J.-K.; Zhang, T.-Y. Discovering a First-Order Phase Transition in the Li-CeO₂ System. *Nano Lett.* **2017**, *17*, 1282–1288. [[CrossRef](#)] [[PubMed](#)]